AIAA JOURNAL
Vol. 49, No. 1, January 2011

Boundary Feedback Flow Control: Proportional Control with Potential Application to Aero-Optics

Marlyn Y. Andino,* Ryan D. Wallace,* and Mark. N. Glauser†
Syracuse University, Syracuse, New York 13211
R. Chris Camphouse‡
Sandia National Laboratories, Carlsbad, New Mexico 88220
and
Ryan F. Schmit§ and James H. Myatt§
U.S. Air Force Research Laboratory, Wright-Patterson Air Force Base, Ohio 45433

DOI: 10.2514/1.44742

A large percentage of the losses in performance and effectiveness of airborne optical systems are caused by turbulence. In an effort to reduce these adverse effects in airborne optical systems, we are exploring the use of both open- and closed-loop flow control over a cylindrical turret. A series of experiments were performed at a Reynolds number of 2×10^6, based on the turret's diameter and freestream velocity, which corresponds to a Mach number of 0.3. The three-dimensional turret contained an actuation system that consists of 17 synthetic jets placed upstream from the leading edge of the aperture. Initially, a large database containing no control and open-loop control was obtained. These data sets provide a rich ensemble for the development and application of a simple proportional closed-loop control with the use of proper orthogonal decomposition. Surface pressure measurements were acquired across the aperture region for all cases studied. Results from the open-loop test demonstrate a reduction of 19.6% in the root-mean-square values when compared to the baseline case. The closed-loop flow control results show that the root-mean-square pressure fluctuations are reduced by 25.7%, the integral scales are significantly reduced, and the flow is driven toward homogeneity.

Nomenclature

A_{jet}	=	area of jet's exit
A_∞	=	frontal area of the turret
$a_m(t)$	=	temporal coefficients baseline proper orthogonal decomposition
$b_m(t)$	=	temporal coefficients lumped proper orthogonal decomposition
C_μ	=	momentum coefficient
$c_n(t)$	=	temporal coefficients split proper orthogonal decomposition
f	=	actuators' driving frequency
f^+	=	nondimensional frequency
M	=	number of modes
p	=	fluctuating pressure
p'	=	root-mean-square pressure
q_∞	=	freestream dynamic pressure
U_∞	=	freestream velocity
u, v	=	streamwise and cross-stream velocities
u_{jet}	=	jet average exit velocity
x, y	=	streamwise and cross-stream coordinates
x_s	=	length of separation over the model
$\xi_n(x, y)$	=	actuator nth mode
ρ	=	density, kg
τ	=	time lag
$\phi_m(x, y)$	=	lumped mth mode
$\varphi_m(x, y)$	=	baseline mth mode

Subscripts

B	=	baseline proper orthogonal decomposition
L	=	lumped proper orthogonal decomposition
m	=	mode number

Presented as Papers 2008-4216 and 2007-4217 at the 39th Plasmadynamics and Lasers Conference, Seattle, WA, 23–26 June 2008; received 3 April 2009; revision received 3 June 2010; accepted for publication 7 June 2010.

*Ph.D. Candidate, Mechanical and Aerospace Engineering Department. Student Member AIAA.
†Professor, Mechanical and Aerospace Engineering Department. Associate Fellow AIAA.
‡Research Scientist, Performance Assessment and Decision Analysis Department. Senior Member AIAA.
§Research Scientist, Air Vehicles Directorate. Associate Fellow AIAA.

I. Introduction

AIRBORNE optical systems are affected by turbulence. As a planar optical wavefront travels through a fully turbulent flowfield, it encounters large density fluctuations and a variant index of refraction, causing aberrations in the wavefront, as shown in Fig. 1. Energy is scattered at wide angles, causing a decrease in the far-field intensity. These effects are adverse; for example, the performance of a laser beam projected through such a turbulent flowfield will be diminished [1–5]. The effects caused by the turbulent flow phenomena in the near field (such as separated flows, boundary layers, and shear layers) are classified as the aero-optic problem [6]. Similarly, the far-field aberrations are called the atmospheric propagation problem [6]. A measure of the optical aberrations is typically done in terms of variations of the beam's optical path length over the aperture [1]. The optical path length is defined as an integration of the index of refraction, $n(r, \theta, t)$, in the direction of propagation. Commonly, a measure of the optical path difference (OPD) is performed, defined as the relative difference between the optical path length and its spatial average across the aperture, from which the root-mean-square value (OPD_{rms}) is extracted.

Several studies over the past three decades have achieved a lot of progress in the mitigation of atmospheric propagation distortions using adaptive optics. Such systems use a conjugate wavefront that compensates for the losses based on the aberrations present. The aero-optic problem, on the other hand, requires a different type of approach, given the temporal bandwidth [1] of these events. A study

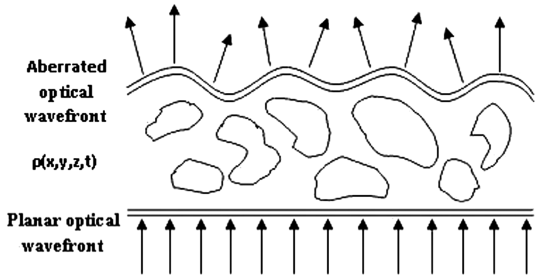

Fig. 1 Planar wavefront as it travels through a flowfield with large density fluctuations.

of weakly compressible shear layers [4] demonstrates that large-scale structures produce large optical distortions. That study suggests two strategies to mitigate the optical disturbances: the regularization of the vortical structures and thickening of the boundary layer to delay the development of large-scale structures past the optical aperture. Recent studies [5] demonstrated that the area of optical distortion is mostly driven by the middle- and low-speed sides of the shear layer. Therefore, in the context of this paper, these optical aberrations should be receptive to flow control upstream of separation.

Previous work to improve the aero-optic problem used techniques such as adaptive optic control, passive flow control, and active open-loop flow control. Adaptive optics [7] was used to sustain laser intensity instead of altering the flow around the turret; the beam was adapted to account for the flow conditions by means of a morphing lens. Real-time data were fed back to a deformable mirror that contorted to match flow conditions and keep the laser focused. This method shows much promise and is still being refined. In a passive flow control experiment [8], vortex generators were mounted fore of a 2-D turret to alter the flow over the turret. Results showed an improvement in the optical environment for small aperture angles (97–105 deg) using small vortex generators. In the cases of higher angles these devices presented an unsatisfactory result, having no impact or increasing the optical aberrations. Large vortex generators presented some promising trends for higher aperture angles, keeping the OPD_{rms} almost constant.

A computational study [3] over a backward-facing step evaluated the impact of flow control on flowfield characteristics and laser distortions. The flow control was implemented using microjets placed upstream of the step. A reduction of the optical distortions was found for the two locations studied: one before and one within the reattachment region. Flow control produced a reduction in the length scales, mixing enhancement, and an elongation of the recirculation region.

Work [9] that included a study of open-loop flow control and corresponding aero-optics using synthetic jets in a meridional array to actively control the wake region of the turret. The effectiveness of the actuation system was based on separation delay and the suppression of flow fluctuations. The application of high-frequency actuation was found to be successful, mitigating the fluctuations and delaying separation along the central domain of the turret. This high-frequency actuation caused improvement in the optical distortions.

Recent work using closed-loop flow control has shown the ability to alter the flow to achieve desired flow characteristics. A study of the separated flow over a NACA 4412 presented a method that combines the proper orthogonal decomposition (POD) and the modified linear stochastic estimation (mLSE) that is sufficient for estimating the velocity field over a NACA 4412 airfoil using only surface pressure data [10]. Further development of this work was expanded in a closed-loop flow control experiment [11] done in the Syracuse University wind tunnel with a NACA 4412 airfoil. Pressure-based temporal POD/mLSE coefficients were obtained and fed back in real time via a proportional control system. The output of the synthetic jet actuators, located near the leading edge of the airfoil, was proportional to the low-dimensional POD time-dependent coefficients. Without control, the airfoil would fully stall at an angle of attack of 16 deg, but with control, stall did not fully occur until an angle of attack of 18 deg. The use of proportional closed-loop feedback flow control system effectively delayed the onset of stall at high angles of attack by altering the characteristics of the flow [12].

Our main long-term objective is to develop a robust real-time closed-loop flow control system capable of reducing the aero-optics effects. In this paper we present results toward this goal. Unsteady surface pressure measurements on a three-dimensional turret are obtained, allowing us to characterize the separated flow over the turret's aperture and develop our control strategies. The experiments were performed at a Reynolds number of 2×10^6, corresponding to a Mach number of 0.3, based on the turret's diameter and freestream velocity. The 3-D turret has a diameter of 30.48 cm with a flat aperture of 14.22 cm in diameter. Our actuation system consists of 17 synthetic jets created by 34 piezoelectric disks. The actuation system was placed 2.54 cm upstream from the leading edge of the aperture, and various actuation cases were tested to evaluate the effects of the flow control over the aperture area. A large database has been built that includes various flow states, including baseline, 13 open-loop control, and six closed-loop control. We use these data sets to provide a rich POD basis for our simple proportional control and, in general, to quantify the effects of the control, both open loop and closed loop. In this paper results from surface pressure measurements are presented. We examine results from both the autocorrelation functions and spectra of these pressure fluctuations. To help us do so, we look specifically at the influence of the control on the integral time scales, shapes of the correlations, spectral content, and p' surface pressure. Even when the measurements performed are not direct measures of the aero-optics, literature [8,9] suggests that there is a strong relationship between them and the optical quality of the flow.

II. Experimental Setup

A. Facility

The Subsonic Aerodynamic Research Laboratory (SARL) wind tunnel at Wright-Patterson Air Force Base is an open-loop wind tunnel with a test section that is 2.13 m wide by 3.05 m high by 4.57 m long. The wind tunnel has a capacity to generate flows ranging from Mach numbers 0.1 to 0.5. Tests were run at Mach numbers 0.3 to 0.4, corresponding to Reynolds numbers of 2×10^6 to 2.8×10^6, respectively, based on the turret's diameter and freestream velocity. The SARL's test section is equipped with Plexiglas windows all around the test section, as shown in Fig. 2.

B. Test Model

The turret consists of a hemisphere on a cylindrical base, as shown in Fig. 3a. The hemisphere is 30.48 cm in diameter with a 14.22 cm flat aperture at the top of the hemisphere. The aperture is set to have a boresight angle of 120 deg, with respect to the incoming flow, facing downstream. This angle was fixed for all the data discussed in this paper. A 12.7-cm-high cylindrical base is used to mount and adjust the boresight angle of the hemisphere. Attached underneath the turret is a splitter plate that is 0.91 m wide by 1.52 m long. The use of a splitter plate allows us to have a smaller aspect ratio between the cylindrical base height to the radius of the model. It also reduces the impact of the structures that develop at the pedestal base with the turret's wake.

On the upstream surface of the turret's aperture there is an actuation bank with an array of 17 oscillatory jets. The actuation bank for the turret was designed in a modular housing, as shown in Fig. 4a, and was built using stereolithography with a WaterShed 11120 resin. The synthetic jets [13,14] use two ceramic piezoelectric diaphragms sealed into a cavity with only a thin slot, 0.5 mm wide and 15.24 mm long, to move the air through. The thickness of the cavity is about 2 mm, giving a volume of 1.14×10^{-6} m^3. The cavity of the synthetic jets was designed using the Helmholtz resonator principle by setting the resonance frequency of the diaphragm equal to the Helmholtz frequency. The jets' exits are oriented at 30 deg with respect to the surface of the hemisphere [15], which makes it almost tangent to the flow. The diaphragms are Omega Piezo Technologies model OPT-BD-27T-2.6A1, as shown in Fig. 4, with a diameter of 27 mm and a resonant frequency of 2.6 ± 0.3 kHz. A calibration of

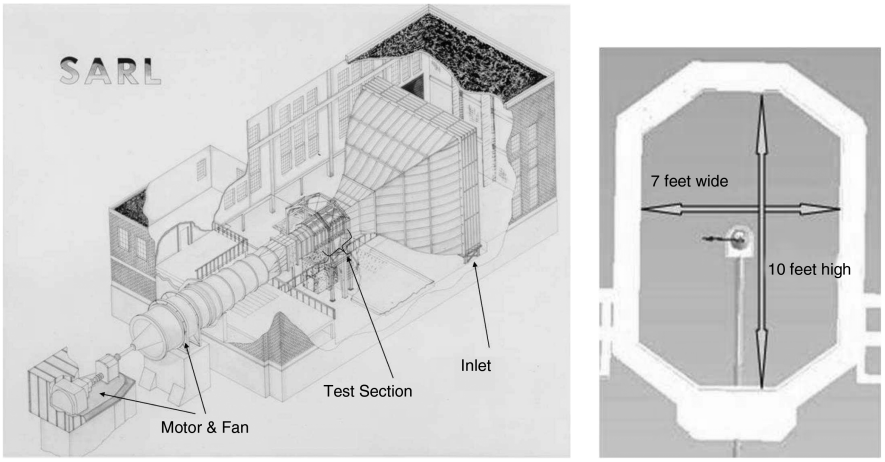

a) Isometric view of the wind tunnel b) Cross-sectional view

Fig. 2 SARL at Wright-Patterson Air Force Base, Ohio.

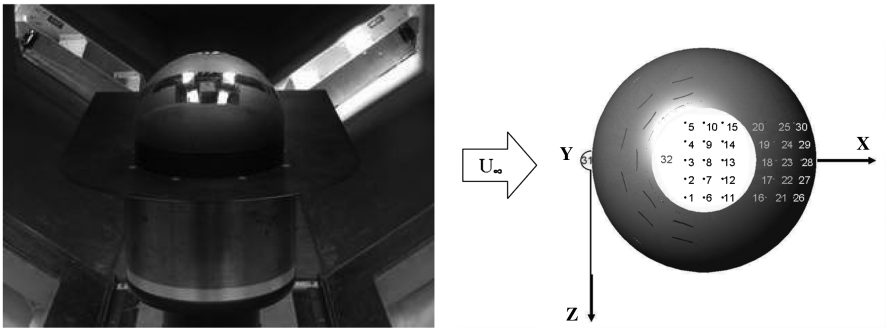

a) Frontal view of SARL's turret configuration b) Coordinate system and pressure sensors distribution (refer to table 2 for specific locations in span)

Fig. 3 SARL's test-article setup. Refer to Table 2 for specific locations in the span.

the actuation system was performed by measuring the exit velocity of the synthetic jets at various actuation frequencies, around the resonant frequency of the piezoelectric disks, and amplitudes using a hot-wire system. Figure 5 presents the actuators' responses using a pure sine wave. Using results obtained from calibration, three carrier frequencies were selected to drive the actuators and obtain a uniform exit velocity from the actuation bank. An average exit velocity of 50 m/s (measured at the center of the slot) is found at these frequencies for an amplitude of ±22.5 V (after amplification).

Dynamic surface pressure measurements were taken using 32 acoustic ICP® PCB Piezoelectronics sensors (model 103B01) distributed along the surface of the turret model. On the flat area or aperture, 16 sensors were placed with a 2.54 cm spacing between them that formed three rows containing five sensors per row. Another

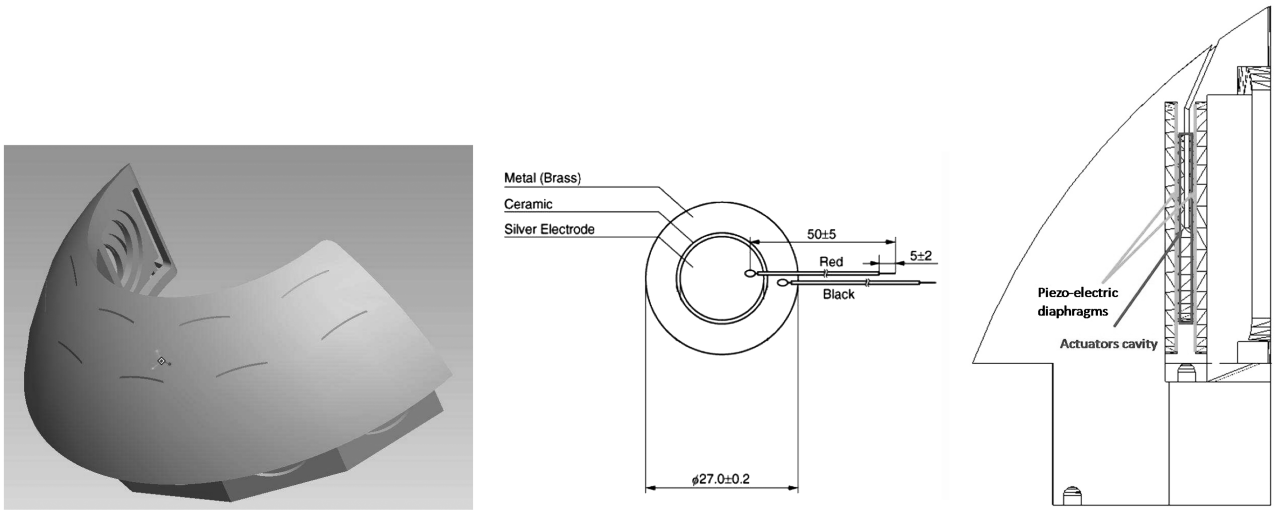

a) b) c)

Fig. 4 Actuation bank: a) isometric view, b) ceramic piezoelectric actuator disk of 27 mm, and c) cross-sectional view of a synthetic jet.

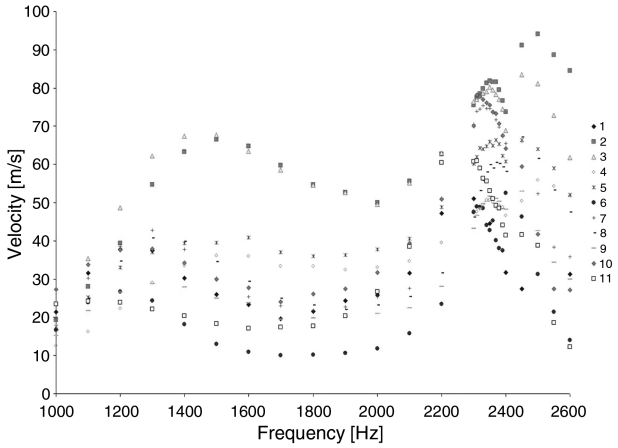

Fig. 5 Exit velocity for the synthetic jets at various frequencies when driven with a pure sine wave.

15 sensors were placed past the trailing edge of the aperture with the same spacing in the cross-stream direction and placed at 10 deg between each row in the freestream direction (see Fig. 3b). The rationale behind the sensors placed in the aperture is to study and understand the flow structures that develop in this area and to look at the effect of actuation on them. We understand that in the real-life application no sensor can be placed on the optical aperture. The acoustic ICP sensors have a measurement range of 22.9 kPa, a resolution of 0.138 Pa, and a bandwidth of 5–13 kHz. The sensors are placed 0.16 cm underneath the surface (minimum dimension necessary to ensure the structural integrity of the model in that area) with an adhesive mounting ring of 0.635 mm in thickness, and the diameter of the orifice for each transducer is 0.16 cm. The calibration for the pressure sensors was done by the manufacturer and they provided each of the sensitivity values.

C. Data Acquisition System

The system used to quantify the transducer's signals was a National Instruments PXI-8175 with an 866 MHz embedded controller and 24-bit high-resolution A/D converters and anti-aliasing filters. The PXI included five SCXI-1531 boards of eight-channel ICP accelerometer conditioning modules. These boards have a sample-and-hold circuitry that warranties that the signals keep their phase information. The signals from all 32 transducers were continuously sampled at 8.5 kHz for all tests: baseline, open loop, and closed loop. For the actuation system, six A-303 AALab Systems piezo amplifiers were employed. These provided a gain of 15 to the voltage sent from the National Instruments PXI-8175, resulting in about 45 V peak-to-peak.

III. Closed-Loop Control Methods

Proper orthogonal decomposition [16] based on the snapshot method [17] was applied to pressure data snapshots obtained via transducers over the aperture. Pressure data over the aperture were collected for the baseline flowfield and 13 open-loop actuation cases. Actuated cases included a nearly periodic and pulse-modulated input signals of varying frequencies. An ensemble of 2000 snapshots of the baseline pressure field and 300 snapshots from each open-loop actuated case were taken, resulting in a total of 5900 snapshots. From these snapshots, low-dimensional bases for the pressure field over the aperture were constructed using three different methods.

In the first method, only baseline data were used to construct the POD basis. The resulting expansion of the pressure field over the aperture in terms of the baseline POD basis is in the form

$$p(t,x,y) = \sum_{m=1}^{M_B} a_m(t)\varphi_m(x,y) \tag{1}$$

where M_B denotes the number of baseline modes used in the expansion and $a_m(t)$ is the temporal coefficient for the mth baseline mode $\varphi_m(x,y)$.

For the second method, baseline and actuated snapshots were lumped together, resulting in an ensemble containing both baseline and actuated pressure data. The resulting pressure field expansion is in the form

$$p(t,x,y) = \sum_{m=1}^{M_L} b_m(t)\phi_m(x,y) \tag{2}$$

where M_L denotes the number of lumped POD modes used in the expansion and $b_m(t)$ is the temporal coefficient for the mth lumped mode $\phi_m(x,y)$.

Finally, in the third case, each actuated snapshot was decomposed into a baseline component and an orthogonal component due to actuation. POD was applied separately to the baseline pressure data and actuated data resulting from this decomposition to obtain a split POD [18] basis. The resulting pressure field expansion is of the form

$$p(t,x,y) = \sum_{m=1}^{M_B} a_m(t)\varphi_m(x,y) + \sum_{n=1}^{M_A} c_n(t)\xi_n(x,y) \tag{3}$$

Note that in the split POD expansion in Eq. (3), the baseline pressure field is expanded as in the baseline POD in Eq. (1). For the second sum in split POD, Eq. (3), actuated pressure field information is represented in terms of the actuated POD basis resulting from snapshot decomposition. In this method [Eq. (3)], M_A is the number of actuator modes used in the expansion and $c_n(t)$ is the nth temporal coefficient, corresponding to actuator mode $\xi_n(x,y)$.

A simple proportional feedback controller was implemented in the wind tunnel for each of the three cases above. The control objective was to reduce or eliminate large fluctuations in pressure over the aperture. The controller was of the form

$$u(t) = -K\left[\sum_{i=1}^{M} a_i(t)\right]\sin(2\pi f_0(t-t_0)) \tag{4}$$

In Eq. (4), K is a constant feedback gain, $\{a_i\}_{i=1}^{M}$ are POD temporal coefficients, f_0 is the characteristic frequency of the synthetic jet actuators, and t_0 is a phase shift to compensate for the time delay

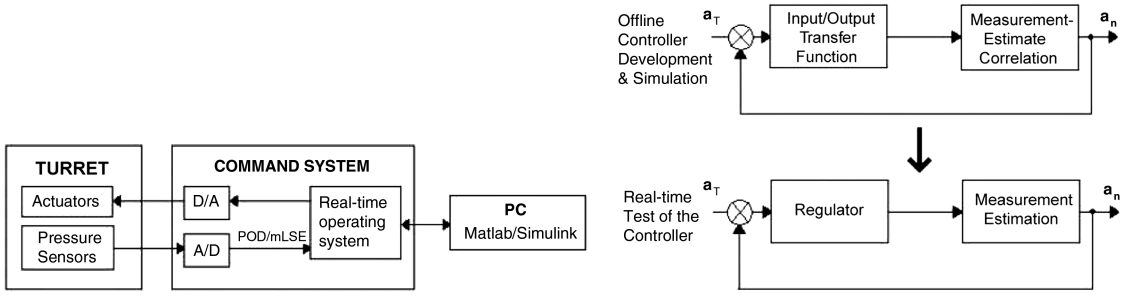

a) Command architecture **b) Controller implementation**

Fig. 6 Control system.

between the actuators and sensors. Figure 6 shows the overall control system.

The temporal coefficients in Eq. (4) were determined in real time during the experiment by projecting sensor pressure data onto the baseline, lumped, or split POD bases. The number of modes chosen in Eq. (4) corresponds to the number of modes necessary for each of the basis construction methods outlined above. In particular, $M = M_B$ for the baseline POD expansion in Eq. (1). For the lumped POD expansion in Eq. (2), $M = M_L$. Finally, $M = M_B + M_A$ for the split POD expansion in Eq. (3). To determine the impact of additional modes on control effectiveness, controllers were constructed using only one mode in expansions in Eqs. (1–3), i.e., $M_B = M_L = M_A = 1$, and the number of modes necessary to capture 99% of the ensemble energy.

IV. Results

A. Open-Loop Control

This work focuses only on the turbulent flow physics with and without control, keeping in mind the suggestions made by researchers in the aero-optics community regarding their needs. In the process of developing a robust closed-loop feedback system, a surface pressure database of various actuated open-loop cases was obtained. The baseline case (no control) is critical for the evaluation of the control effects on the flow dynamics. Open-loop control was then applied to the flow, employing the synthetic jets at their resonant frequency, 2.6 kHz. This carrier frequency was fixed for all the cases studied. The input signal for the actuated cases included a pure sine wave (PSW), modulated sine wave (MSW), and modulated square wave (MSQW), shown in Fig. 7. The duty cycle of the modulated square wave was fixed to 50% and offset to place the low level of the waveform at 0 V. This created an on/off effect in the input signal. Table 1 contains more details about all the cases studied for the open-loop tests. Nondimensional frequencies f^+,

$$f^+ = f\frac{x_s}{U_\infty} \tag{5}$$

ranged from 0.5 to 2. In Eq. (5), f is the frequency of modulation of the input signal, x_s is the length of separation over the test model, and U_∞ is the freestream velocity. For this model, we consider that the length of separation started at the leading edge of the aperture and extended to the back of the aperture, for a total length of 22.6 cm. Even when the separation was three-dimensional, we took this length from the center plane. This provides the largest separation over the body. The average momentum coefficient for this test model produced per synthetic jet was 5.4×10^{-5}. This quantity was calculated using the following equation:

$$C_\mu = \frac{(\rho A u^2)_{\text{jet}}}{(\frac{1}{2}\rho A U^2)_\infty} \tag{6}$$

where ρ is the density of air, A_{jet} is the area of the jet's exit, A_∞ is the frontal area of the turret, and u_{jet} is the synthetic jet average velocity.

Table 1 Open-loop flow control cases studied

Nondimensional frequency	Actuation frequency , Hz
Simple sine wave	
5.12	2600
0.5	250
0.75	375
Modulated sine wave	
1	500
1.25	625
1.5	750
2	1000
0.5	250
0.75	375
Modulated square wave	
1	500
1.25	625
1.5	750
2	1000

Table 2 Pressure sensors location per measurement plane (see Fig. 3b as well)

z, cm	Sensors						
5.08	——	1	6	11	16	21	26
2.54	——	2	7	12	17	22	27
0	32	3	8	13	18	23	28
−2.54	——	4	9	14	19	24	29
−5.08	——	5	10	15	20	25	30

For the purpose of the results presented here, Fig. 3b shows the coordinate system established for the experiments performed using the three-dimensional turret. As mentioned previously, the pressure transducers are distributed and aligned with five planes across the spanwise direction z. The distribution and locations are presented in Table 2. For clarification, sensor 31 was located 30 deg upstream of the stagnation point aligned with the center plane.

Figure 8 shows the unsteady pressure fluctuations for six of the cases studied from sensor 3 located on the aperture of the turret (see Fig. 3b). An examination of the mean-square values of these signals indicates a reduction of $19.6 \pm 6\%$ for the case of $f^+ = 2$. It is interesting that for the high-actuation case, i.e., Figs. 8e and 8f, in which an amplitude-modulation signal is used, the fluctuations decrease, in agreement with the findings of Vukasinovic et al. [9].

We further look at the higher-order moments of the pressure data, such as its root mean square p', skewness s, and kurtosis κ, shown in Table 3. A reduction of $19.6 \pm 6\%$ is observed when the modulated square wave with and $f^+ = 2$ is applied. The skewness is also being shifted toward a normal distribution with all the open-loop cases. The kurtosis presents a reduction of up to $45 \pm 6\%$ in the control cases

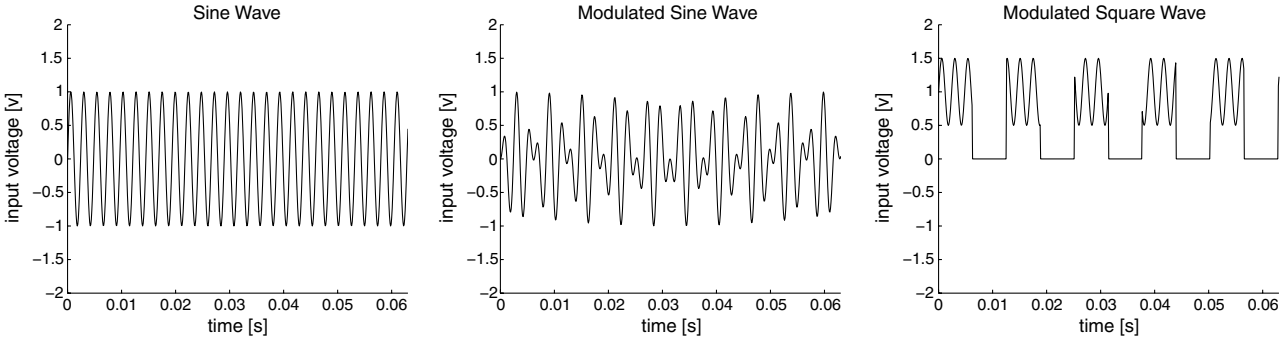

a) Pure sine wave **b) Modulated sine wave** **c) Modulated square wave**

Fig. 7 Excitation input signals.

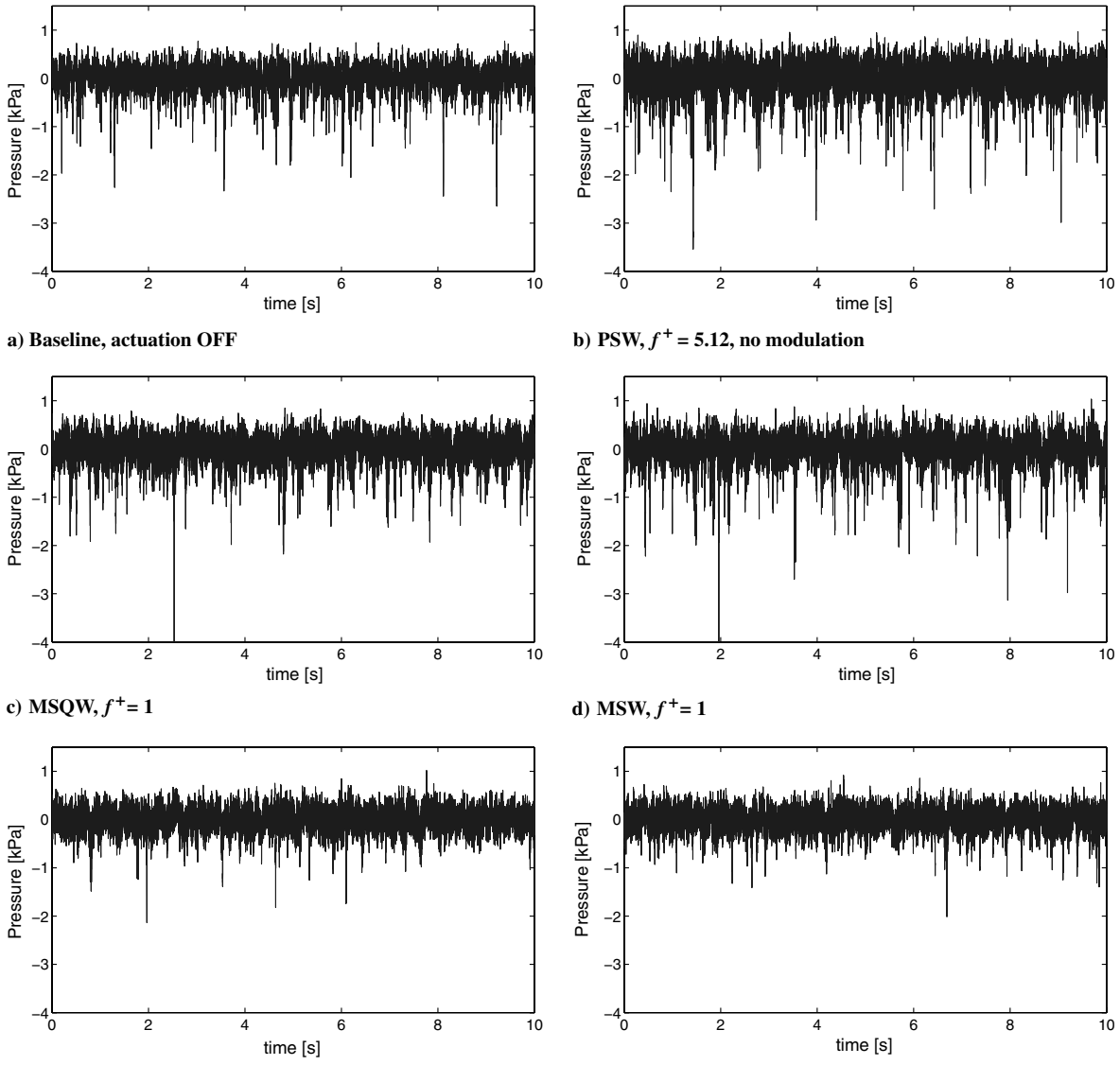

a) Baseline, actuation OFF

b) PSW, $f^+ = 5.12$, no modulation

c) MSQW, $f^+ = 1$

d) MSW, $f^+ = 1$

e) MSQW, $f^+ = 2$

f) MSW, $f^+ = 2$

Fig. 8 Pressure fluctuations at transducer 3 for various forcing frequencies.

with $f^+ = 2$. The open-loop control seems to be imposing a similar size to the structures that develop across the surface of the turret.

Pressure spectra for some sensors along the center plane (i.e., sensors 3, 13, 23, and 31 are the boundary layer) are presented in Fig. 9 for the same six cases presented in Fig. 8. To compute the spectra, the data were divided in 0.25 s record-length windows that provided a total of 280 spectral estimates, resulting in 6% variability (standard rectangular block windows with zero overlap). The sampling frequency of 8.5 kHz provided a resolution of 4 Hz for the pressure spectra. The conversion from kilopascals to decibels was done using a reference pressure of 20×10^{-6} Pa. As expected, the modulated square wave presents a richer frequency spectrum when compared to the modulated sine wave, and in both cases the pressure spectra collapse for all sensors at the center plane. From the pressure level we can infer that for the two cases in which the forcing control was $f^+ = 2$ (Figs. 9c and 9d), there is a slight change in the spectrum pattern. In general, the curves are closer to each other. Even though the modulated square wave is richer in frequency content, the modulated sine wave also does well at organizing the flow by means of homogenization across the turret's surface.

Table 3 Statistics for pressure sensor 3

z	f^+	p', kPa	s	κ
Baseline	0	0.270	−1.236	8.544
PSW	5.12	0.314	−1.120	7.095
MSW	1	0.272	−1.156	7.608
MSQW	1	0.261	−0.973	6.853
MSW	2	0.214	−0.459	4.664
MSQW	2	0.217	−0.489	4.771

The autocorrelation function was computed using the fluctuating pressure from the same location at two different times, t and t', shown in Eq. (7). In this equation, τ represents the time lag $t' - t$. This analysis provides information on the spatial evolution of the time integral scales across the turret's surface. The autocorrelations are shown for all sensors over the three-dimensional turret in Fig. 10. Here, we have only included the actuated cases with an $f^+ = 2$, because those were the cases that presented a maximum reduction in the pressure p' fluctuations:

$$\rho(\tau) = \frac{\overline{p(t)p(t+\tau)}}{\overline{p(t)^2}} \tag{7}$$

The autocorrelations of the surface pressure fluctuations of sensor 3 for the best open-loop cases are shown in Fig. 10a. A slight variation between the baseline and actuated cases can be observed. The baseline autocorrelations for all the sensors across the aperture and back of the turret shown in Fig. 10b exhibit a substantial variation across the turret surface. This demonstrates the three-dimensionality

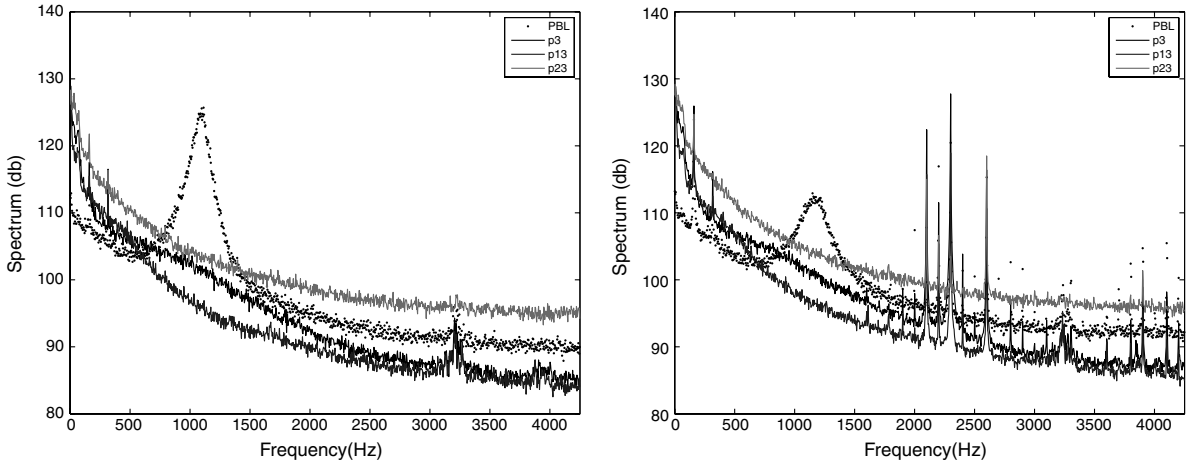

a) Baseline, no actuation

b) PSW, $f^+ = 5.12$, no modulation

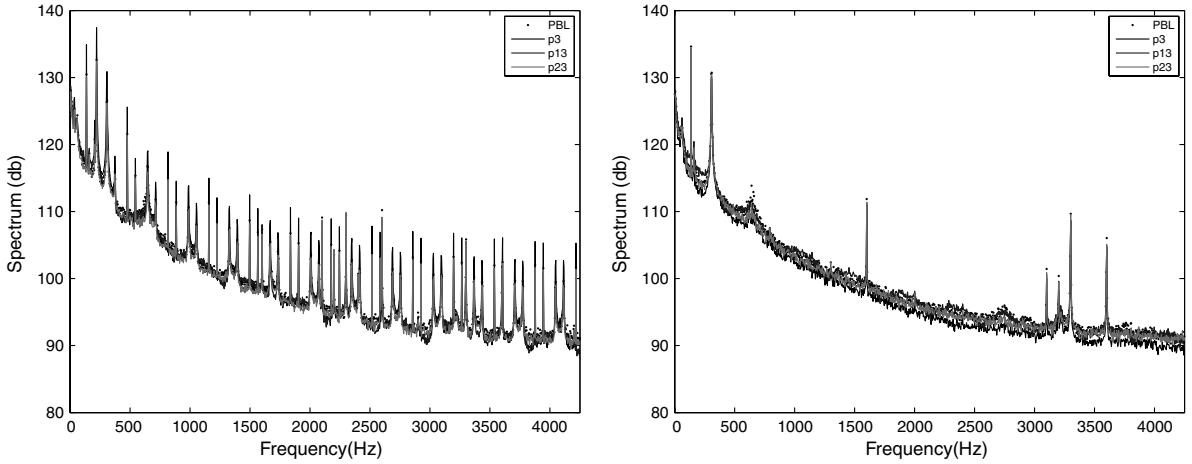

c) MSQW, f^+=2

d) MSW, $f = 1\ kHz$, $f^+ = 2$

Fig. 9 Pressure spectra of the center plane. $z = 0$, for baseline and three high-frequency actuation cases, where PBL is pressure sensor 31.

and turbulent behavior of the flow. When open-loop control is applied using $f^+ = 2$ (Fig. 10c), it appears (except for sensor 13, where we see a large integral time scale) that the forcing is breaking up large structures and driving the flow to a more spatially homogeneous state. These findings agree well with the changes in the higher-order moments with the application of open-loop control. With respect to the autocorrelation from sensor 13, the large scale observed at this location appears to be consistent with the recent work by Morgan and Visbal [19]. They show the development of a large eddy in the same region when they force with an oscillatory excitation. Note, in particular, the cyclic behavior picked up by the sensors on the aperture at the centerline of the turret. Sensors 3 and 8, located on the center of the aperture (see Fig. 3b),present similar cyclic behavior for all actuated cases. The frequency bands of these are at or near the resonant frequency of the piezoelectric disks.

B. Closed-Loop Control

To assure the effectiveness of the feedback controller, it is necessary that dynamics induced by closed-loop actuation be observed by pressure sensors placed in the wind-tunnel model. As shown in Fig. 3b, the turret model incorporates two banks of pressure transducers: one over the optical aperture window and one aft of the aperture window. Baseline and actuated pressure data were collected using both banks of sensors. To gain insight into the most beneficial pressure sensor locations from a controls standpoint, split POD was performed on pressure measurements obtained from each bank of actuators separately. Split POD [18] decomposes actuated data into orthogonal baseline and actuated components via a projection onto a baseline basis. By applying split POD, it was apparent that sensors located in the downstream bank of the aperture were not useful from a feedback control standpoint. When baseline components obtained

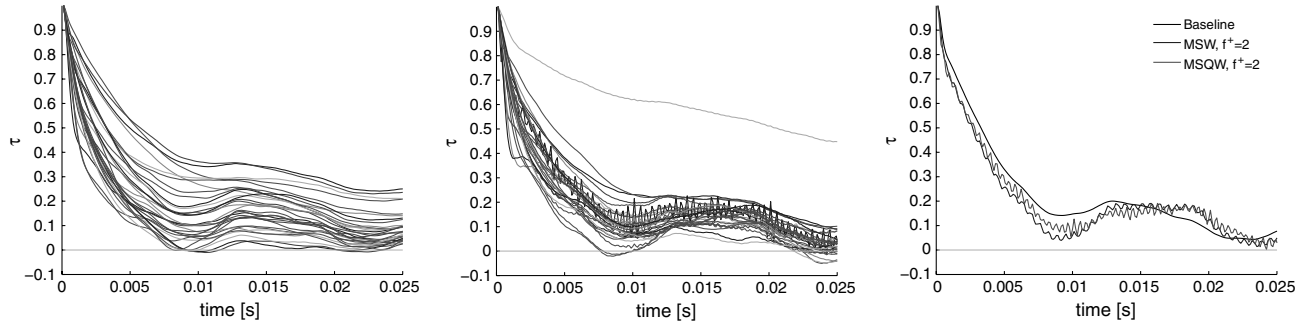

a) Baseline, all sensors

b) MSQW, $f^+ = 2$

c) Selected open-loop cases, sensor 3

Fig. 10 Pressure autocorrelations at $M = 0.3$.

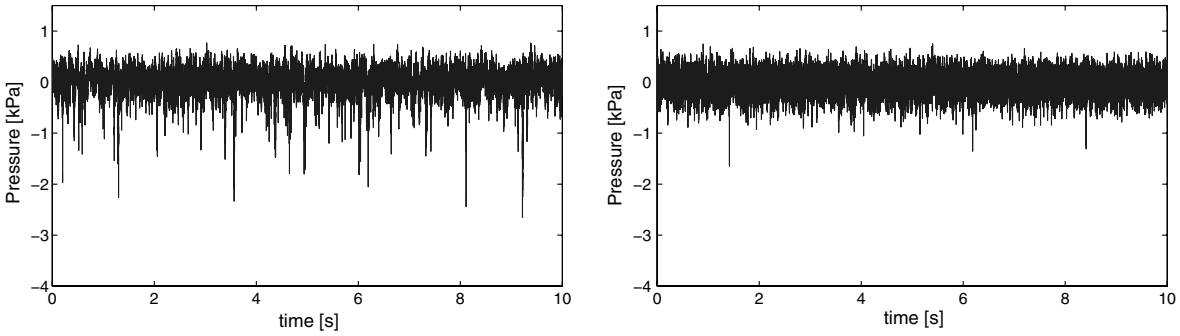

a) No control **b) Split POD**

Fig. 11 Pressure–time series.

via projection were removed from the actuated data at these sensor locations, there was no nontrivial component remaining due to actuation. The actuated data collected at the bank of pressure sensors downstream of the aperture were entirely contained in the span of the baseline basis. Because the flow becomes highly separated downstream of the aperture window, these locations are unable to observe the new dynamics induced by actuation. In effect, these locations are unable to observe improvements or degradation of flowfield unsteadiness in the shear layer due to their location, removing their utility from a feedback control standpoint. When split POD was applied to pressure data taken using the sensor bank over the aperture window, nonzero components due to actuation were obtained after the baseline components were removed from the data. Pressure sensors located over the aperture window very clearly observed new dynamics induced by actuation. As a result, only this bank of sensors was used to develop the control laws previously described. For the closed-loop control, all 32 signals were recorded, but only the 16 sensors located on the aperture were used for the simple proportional feedback control. No time lag was considered for the closed loop, which corresponds to $t_0 = 0$.

During the closed-loop flow control tests the carrier frequency of the synthetic jets was set to the resonant frequency of the cavities that corresponds to the resonant frequency of the piezoelectric disks. The amplitude of the signal was set to stay in a range of ± 3 V before it was sent to the amplifiers. The amplitude modulation was provided via feedback of the time-dependent POD coefficients. These time-dependent POD coefficients were computed offline. A simple multiplication of the coefficients with its corresponding pressure signal was performed in real time to create the feedback signal. Figure 11 shows the pressure–time series data of the baseline and the three different closed-loop POD methods containing 99% of the energy for sensor 3. As shown in Table 4, the results from the pressure data show that there is a reduction in the p' as compared to the baseline case. In fact, the greatest reduction comes from the split POD method, with a reduction of $25.7 \pm 6\%$. All the closed-loop cases demonstrate similar reductions on the root-mean-square values that fall within the statistical uncertainty in the measurements. Table 4 contains more details on the high-order moments of the closed-loop pressure data for sensor 3. It is interesting to note that the closed loop improves on the open loop for all the quantities presented. The skewness for all the closed-loop cases is closer to a Gaussian distribution and the kurtosis is reduced to $60 \pm 6\%$.

Table 4 Statistics for pressure sensor 3

z	Mode	p', kPa	s	κ
Baseline	——	0.270	−1.236	8.544
Baseline POD	1	0.205	−0.319	3.740
Baseline POD	99%	0.203	−0.314	3.685
Lumped POD	1	0.211	−0.250	3.811
Lumped POD	99%	0.208	−0.247	3.416
Split POD	1	0.205	−0.260	3.477
Split POD	99%	0.201	−0.254	3.424

We further investigate the impact of closed loop (again with 99% of the energy) on pressure fluctuations by examining the autocorrelation function $\rho(\tau)$ for each of the pressure transducers, as we did earlier for the open-loop cases. Here, we again show the baseline case (Fig. 12a) for comparison purposes. As described earlier, the autocorrelations for the baseline vary substantially across the upper surface of the turret and aperture. Figure 12b show the autocorrelations from all the pressure sensors signals across the turret for the closed-loop case using the split POD method (99% of the energy). It is important to note the global behavior on the pressure autocorrelations when closed-loop control is applied. Note how the autocorrelations collapse on one another (for example, compare the uncontrolled baseline data and the open-loop results shown in Fig. 10). Figure 12c presents the autocorrelations of sensor 3 for baseline, modulated square wave with $f^+ = 2$, and split POD with 99% of the total energy. It is clearer here that there is a significant reduction in the integral time scale for the closed-loop control results. Similar results are found for all the sensors across the surface of the turret. Clearly, the closed-loop control is homogenizing the flow and driving it to smaller scales. Similar results are obtained using baseline and lumped POD methods.

Although not shown here, when only one POD mode containing 40% energy (as opposed to 99%) is used to feedback, the pressure–time series and autocorrelation results are basically the same as for

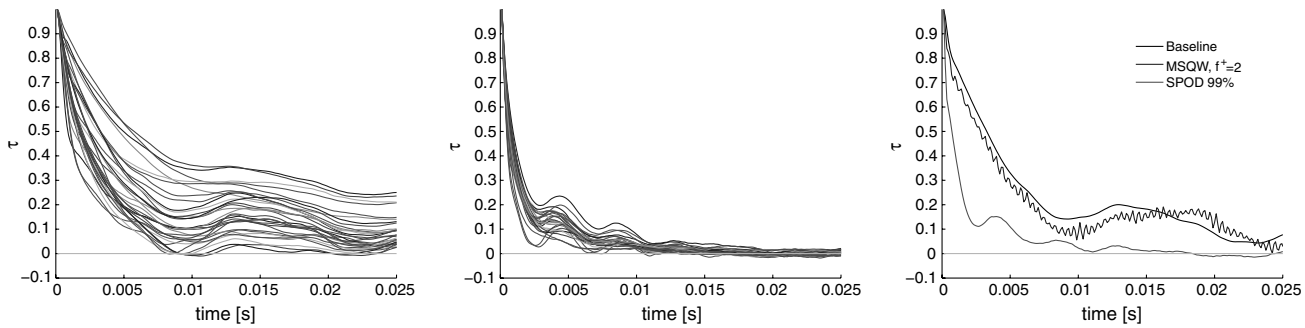

a) Baseline, all sensors **b) Split POD, all sensors** **c) Autocorrelations sensor 3**

Fig. 12 Pressure autocorrelations.

the 99% results shown here. This suggests that low-dimensional models developed for only a few modes may be adequate for closed-loop control for such flows. To achieve 99% of the energy, out of 5900 modes, only 12, 12, and 15 modes are used for baseline, lumped, and split POD, respectively.

V. Conclusions

Open- and closed-loop flow control were applied to a three-dimensional turret using synthetic jets upstream from the leading edge of the aperture. In this paper we focus on surface pressure measurements to quantify the effects of control. We examine results from the autocorrelation function and spectra, looking specifically at the influence of the control on the integral time scales, shapes of the correlations, spectral content, and p' surface pressure fluctuations. Experiments were performed at a Mach number of 0.3, which corresponds to a Reynolds number of 2×10^6. Multiple open-loop control cases were studied by varying the nondimensional frequency f^+ from 0.5 to 2 and in one case the actuators were driven only at their resonance frequency. Pressure measurements are taken on the aperture and back of the turret. The rationale behind the sensors placed in the aperture is to study and understand the flow structures that develop in this area and look at the effects of actuation on them, keeping in mind that in the real-life application no sensor can be placed along the beam's aperture. Surface pressure results showed that open-loop control is able to somewhat homogenize the flow and reduce the pressure fluctuations by about 19%.

Pressure results from closed-loop control tests demonstrated a reduction in the pressure fluctuations of 25% and significant reduction in the spatial gradient of the integral scales across the surface of the turret. This reduction indicates that the closed-loop control is driving the flow toward homogeneity. This work demonstrated how a simple proportional controller based on surface pressure alone, can alter flow characteristics and reduce the fluctuations that possibly lead to the degeneration of light intensity. The change in the flow characteristics between the no control to closed-loop control indicates that the actuators have sufficient control authority and the pressure transducers on the aperture obtained adequate observability. Future studies will include redistribution of the pressure transducers located behind the aperture guided on computational fluid dynamics analysis to achieve better observability.

This work, as the first approach from this group, has established the ability of the flow control approach to be effective in reducing the turbulent time and length scales all across the turret using closed-loop flow control. The various closed-loop control results showed no significant differences (99% energy baseline, lumped, split, and one-mode feedback). We note here that the simple proportional feedback controller employed in this work is not model-based. The development of a dynamical turret flow model and its subsequent use for control design may better flush out advantages gained by the use of each particular POD method considered in this study.

Further analysis of both flow and optics data will be done. This will incorporate velocity-pressure correlations and mathematical tools such as proper orthogonal decomposition [16] and modified linear stochastic measurements [20] to construct a low-dimensional velocity-based closed-loop flow control model to estimate the flow states in real time [12]. Analysis of the Malley probe data will show more conclusively how the flow control affects the performance of the laser beam. Additional sources of flow disturbances, such as dynamic pitching and yawing of the turret hemisphere, are currently ongoing.

Acknowledgments

The authors gratefully acknowledge the support of the National Science Foundation through the Central New York–Puerto Rico Alliance for Graduate Education and the Professoriate and the U.S. Air Force Office of Scientific Research, John Schmisseur, Project Manager.

References

[1] Jumper, E. J., and Fitzgerald, E. J., "Recent Advances in Aero-Optics," *Progress in Aerospace Sciences*, Vol. 37, No. 3, 2001, pp. 229–339. doi:10.1016/S0376-0421(01)00008-2

[2] Gordeyev, S., Hayden, T. E., and Jumper, E. J., "Aero-Optical and Hot-Wire Measurements of the Flow Around the Hemispherical Turret with a Flat Window," AIAA Paper 2004-2450, June 2004.

[3] Arunajatesan, S., Sinha, N., and Kannepalli, C., "Analysis of Length Scale Effects in Distortions of Laser Beams Propagating Through Turbulent Flows," AIAA Paper 2006-3071, June 2006.

[4] Fitzgerald, E. J., and Jumper, E. J., "The Optical Distortion Mechanism in a Nearly Incompressible Free Shear Layer," *Journal of Fluid Mechanics*, Vol. 512, 2004, pp. 153–189. doi:10.1017/S0022112004009553

[5] Gordeyev, S., Hayden, T., and Jumper, E., "Aero-Optical and Flow Measurements over a Flat-Windowed Turret," *AIAA Journal*, Vol. 45, No. 2, 2007, pp. 347–357. doi:10.2514/1.24468

[6] Gilbert, K. G., "Aero-Optical Overview," *Aero-Optical Phenomena*, edited by K. G. Gilbert, and L. J. Otten, Vol. 80, Progress in Astronautics and Aeronautics, AIAA, New York, 1982.

[7] Nightingale, A. M., Goodwine, B., Lemmon, M., and Jumper, E. J., "Feedforward Adaptive-Optic System Identification Analysis for Mitigating Aero-Optic Disturbances," AIAA Paper 2007-4013, June 2007.

[8] Gordeyev, S., Jumper, E. J., Ng, T., and Cain, A. B., "The Optical Environment of a Cylindrical Turret with a Flat Window and the Impact of Passive Control Devices," AIAA Paper 2005-4657, June 2005.

[9] Vukasinovic, B., Glezer, A., Gordeyev, S., Jumper, E., and Kibens, V., "Active Control and Optical Diagnostics of the Flow over a Hemispherical Turret," AIAA Paper 2008-0598, Jan. 2008.

[10] Glauser, M. N., Higuchi, H., Ausseur, J., Pinier, J., and Carlson, H., "Feedback Control of Separated Flows," AIAA Paper 2004-2521, June 2004.

[11] Ausseur, J. M., Pinier, J. T., Glauser, M. N., Higuchi, H., and Carlson, H., "Controller Development for Closed-Loop Feedback Control of Flows," AIAA Paper 2005-5264, June 2005.

[12] Pinier, J. T., Ausseur, J. M., Glauser, M. N., and Higuchi, H., "Proportional Closed-Loop Feedback Control of Flow Separation," *AIAA Journal*, Vol. 45, No. 1, 2007, pp. 181–190. doi:10.2514/1.23465

[13] Amitay, M., and Glezer, A., "Controlled Transient of Flow Reattachment over Stalled Airfoils," *International Journal of Heat and Fluid Flow*, Vol. 23, 2002, pp. 690–699. doi:10.1016/S0142-727X(02)00165-0

[14] Smith, D. R., "Interactions of a Synthetic Jet with Crossflow Boundary Layer," *AIAA Journal*, Vol. 40, No. 11, 2002, pp. 2277–2288. doi:10.2514/2.1564

[15] Yehoshua, T., and Seifert, A., "Boundary Condition Effects on Oscillatory Momentum Generators," AIAA Paper 2003-3710, June 2003.

[16] Lumley, J. L., "The Structure of Inhomogeneous Turbulence," *Atmospheric Turbulence and Radio Wave Propagation*, edited by A. M. Yaglom, and V. I. Tatarski, 1967, pp. 166–178.

[17] Sirovich, L., "Turbulence and the Dynamics of Coherent Structures, Parts I–III," *Quarterly of Applied Mathematics*, Vol. 45, 1987, pp. 561–590.

[18] Camphouse, R. C., Myatt, J. H., Schmit, R. F., Glauser, M. N., Ausseur, J. M., Andino, M. Y., and Wallace, R. D., "A Snapshot Decomposition Method for Reduced Order Model and Boundary Feedback Control," AIAA Paper 2008-4195, June 2008.

[19] Morgan, P. E., and Visbal, M. R., "Numerical Simulations Investigating Control of Flow over a Turret," AIAA Paper 2009-0574, Jan. 2009.

[20] Bonnet, J. P., Cole, D. R., Delville, Glasuer, M. N., and Ukeiley, L. S., "Stochastic Estimation and Proper Orthogonal Decomposition: Complementary Techniques for Identifying Structures," *Experiments in Fluids*, Vol. 17, No. 5, 1994, pp. 307–314. doi:10.1007/BF01874409

A. Tumin
Associate Editor